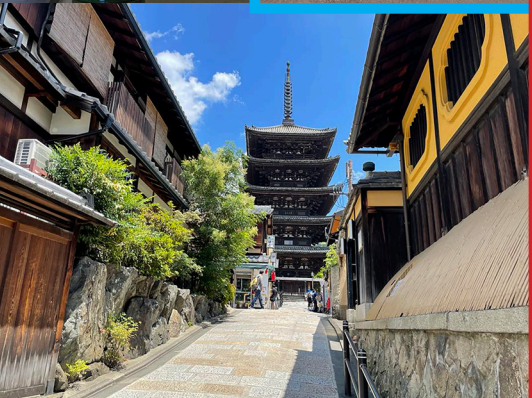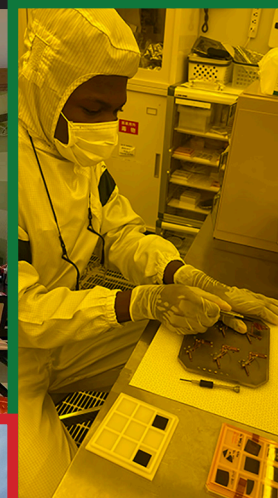# Cornell NanoScale Science & Technology Facility

# 2023 JAPAN PROGRAMS FINAL REPORTS

# 2023 CNF Japan Programs Final Reports

# TABLE OF CONTENTS

# Fabrication of Graphene Moiré Superlattice Devices

**2023 GQL IRTE Intern: Desvaun Drummond**

**2023 GQL IRTE Intern Affiliation: Electrical Engineering, Howard University**

**2023 GQL IRTE Principal Investigator: Dr. Takuya Iwasaki**

**2023 GQL IRTE Program Location: National Institute for Materials Science (NIMS), Tsukuba, Ibaraki, Japan**

**Primary Sources of Research Funding: 2023 Global Quantum Leap International Research Training Experience (GQL IRTE) Program**

**Contact: desvaun@gmail.com, iwasaki.takuya@nims.go.jp**

**Website: https://cnf.cornell.edu/education/reu/2023**

## Abstract:

Graphene, a two-dimensional (2D) sheet with carbon atoms arranged in a honeycomb lattice, has attracted attention because of its unique electronic properties. When graphene is stacked on hexagonal 2D materials such as graphene or hexagonal boron nitride (hBN), an interference pattern (moiré pattern) emerges in the stacking structure due to a small lattice constant mismatch or rotational misalignment. This moire superlattice has a long-period structure, giving rise to intriguing emergent properties in the materials beyond the original band structure of parent layers. To utilize such properties for device applications, investigation of fundamental properties in moiré superlattices should be imperative.

## Summary of Research:

Graphene and hBN were grown from exfoliating kish graphite and hBN flakes using scotch tape. An original transfer station was used to assemble the graphene/hBN heterostructures, and an atomic force microscopy (AFM) was used to scan the heterostructure. A viscoelastic polymer stamp is required for the transfer process, as it minimizes the possible contamination of graphene. Figure 1 shows the final stamps to be used for assembling the heterostructure.

Once the heterostructures are fabricated using the transfer station, thermal annealing was carried out in a vacuum chamber with argon as a protection gas, and at an elevated temperature of 400°C. This process helps to reduce the bubbles around the surface of the graphene in the heterostructure. Bubbles should be avoided as they can degrade the electronic transport property and the device performance by acting as charge traps or scattering centers. The completed heterostructure after annealing is showed in Figure 2, where the outline of graphene can be seen in the middle of the heterostructure.

After annealing, the graphene field effect transistor was fabricated in the NIMS Sengen cleanroom using techniques such as electron-beam lithography, reactive ion etching, and photoresist coating. The device was designed using AutoCAD, where contact electrodes, pads, and Hall bar were outlined in order to test the electrical response of the device after fabrication. The final structure after fabrication is showed in Figure 3, where two devices were placed on the heterostructure.

The final step of the project was to demonstrate the evidence of graphene in the device by testing the device mobility. Using a probe station at room temperature, as shown in Figure 4, this tool can measure the electrical characteristics of a device and confirm the presence of graphene. Additionally, the Keysight B2901A precision source / measure unit (SMU) was used with the probe station. This tool is a 1-channel, compact, and cost-effective benchtop SMU with the capability to source and measure both voltage and current.

## Conclusions and Future Steps:

Our results proved consistent with the standard mobility of graphene. However, the mobility of Device A was much lower than Device B. The exact cause of this difference is unknown, but we were still able to demonstrate evidence of graphene's ambipolar characteristics and high carrier mobility and we fabricated high-quality heterostructure devices for this experiment. Future steps are to test the device at low temperature, around 1.5 K, and perform quantum hall effect measurements.
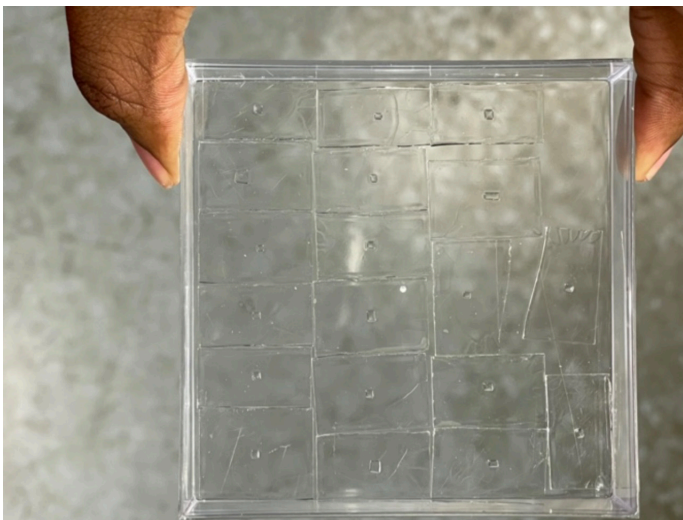
## Acknowledgements:

*Figure 1: Viscoelastic polymer stamps.*
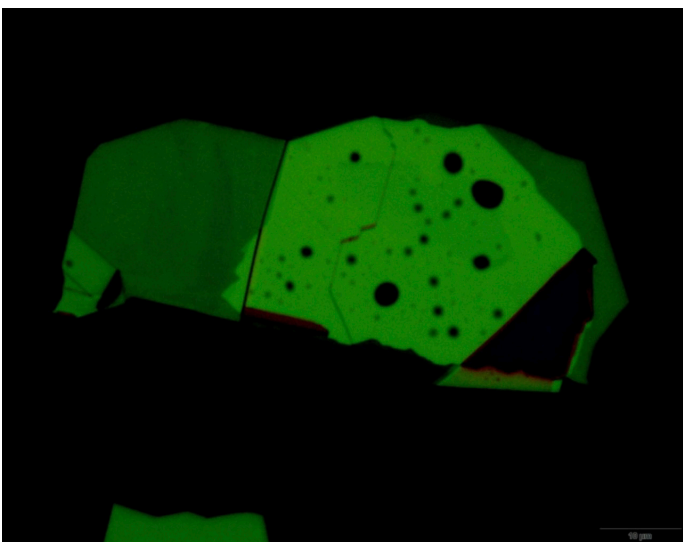


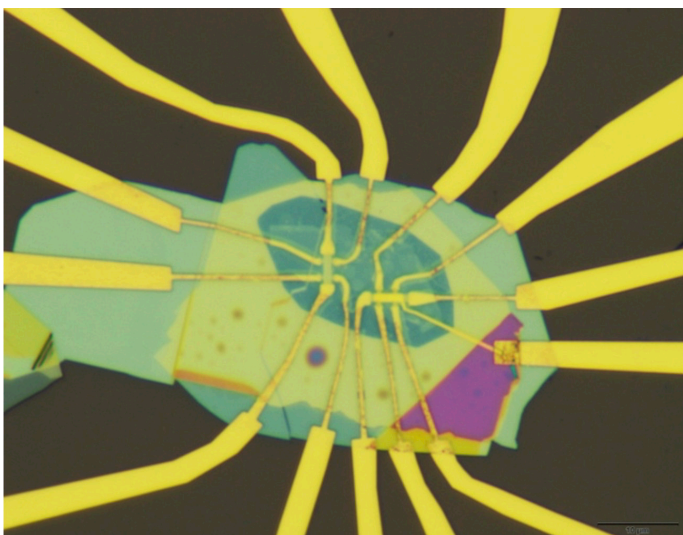*Figure 2: Image of fabricated graphene/hBN heterostructure after thermal annealing.*



*Figure 3: Fabricated graphene FET device.*
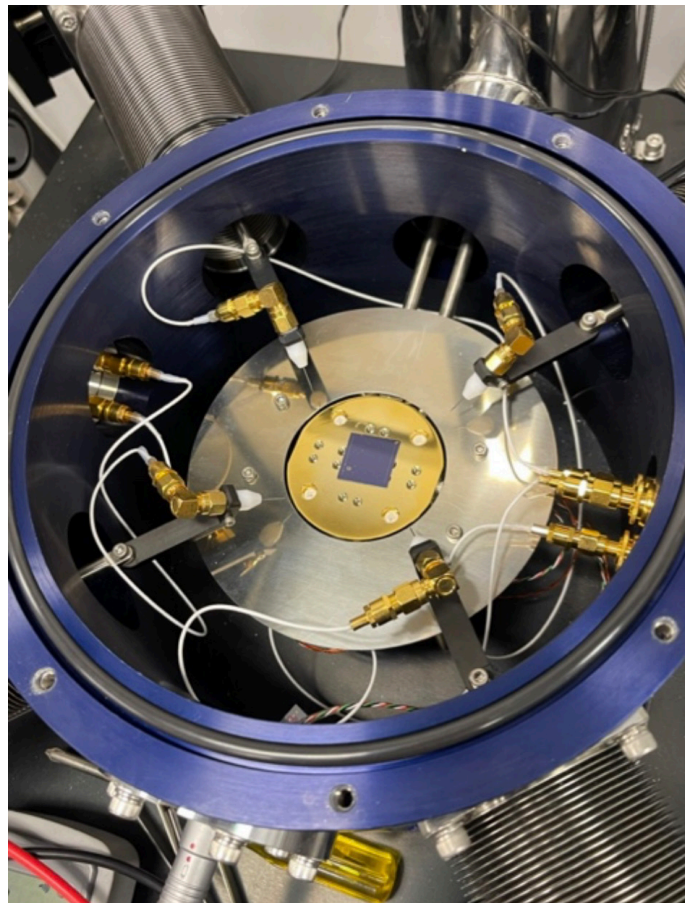


*Figure 4: Probe station.*

## References:

[1]  Zhang, Y., Tang, TT., Girit, C., et al. Direct observation of a widely tunable bandgap in bilayer graphene. Nature 459, 820-823 (2009). https://doi.org/10.1038/nature08105.

[2]  Dean, C., Young, A., Meric, I., et al. Boron nitride substrates for high-quality graphene electronics. Nature Nanotech 5, 722-726 (2010). https://doi.org/10.1038/nnano.2010.172.

[3]  Geim, A., Grigorieva, I. Van der Waals heterostructures. Nature 499, 419-425 (2013). https://doi.org/10.1038/nature12385.

[4]  Wang, D., Chen, G., Li, Chaokai, et al. Thermally Induced Graphene Rotation on Hexagonal Boron Nitride (2016). Physical Review Letters. 116. 10.1103/PhysRevLett.116.126101.

[5]  Iwasaki, T., Morita, Y., Watanabe, K., Taniguchi, T. Dual-gated hBN/bilayer graphene superlattices and the mapping of the energy gap at the charge neutrality point (2022). 10.48550/arXiv.2206.05401.

[6]  Iwasaki, T., Endo, K., Watanabe, E., et al. Bubble-Free Transfer Technique for High-Quality Graphene/Hexagonal Boron Nitride van der Waals Heterostructures. ACS Applied Materials & Interfaces 2020. 12. 10.1021/acsami.9b19191.

# Theory and Simulation of Lateral Heterostructures of 2D Materials

**2023 GQL IRTE Intern: Saisrinivas Gudivada**

**2023 GQL IRTE Intern Affiliation: Physics and Applied Math, University of California, Berkeley**

**2023 GQL IRTE Principal Investigator: Dr. Toshikaze Kariyado**

**2023 GQL IRTE Program Location: National Institute for Materials Science (NIMS), Tsukuba, Ibaraki, Japan**

Primary Sources of Research Funding: 2023 Global Quantum Leap
International Research Training Experience (GQL IRTE) Program

Contact: sritheg@berkeley.edu, kariyado.toshikaze@nims.go.jp

Website: https://cnf.cornell.edu/education/reu/2023

## Abstract:

The electronic structure of two types of lateral heterostructures — composed of $MoSe_2$ and $WSe_2$, and $NbSe_2$ and $ReSe_2$ — were analyzed, and band structure calculations were conducted on two types of heterostructure patterns for both compositions. Changing the $MoSe_2$ and $WSe_2$ heterostructures had minimal impact on the band gap. On the other hand, there was a noticeable decrease in the band gap when switching between the $NbSe_2$ and $ReSe_2$ heterostructures.

## Summary of Research:

Two-dimensional (2D) materials are a class of compounds that have risen in popularity over the past half-century thanks to their extensive list of fascinating phenomena and wide range of tunable properties that make them excellent candidates for many applications: from biosensing to quantum computing. This work computationally explores the use of lateral heterostructures to engineer tunable properties in the band structure of these materials.

## Methodology:

A vital step in creating heterostructures is determining what combinations of materials to use in each material system. There are many types of 2D materials with varying geometries and primitive unit cell sizes, so picking compounds in the same space group (geometry) that are close together in lattice constant and cell height prevents strain or defects (especially in experimental applications). This study focuses on two types of lateral heterostructure groups based on transition metal dichalcogenides (TMDs): the first composed of molybdenum diselenide and tungsten diselenide ($MoSe_2$ and $WSe_2$) and the second of niobium diselenide and rhenium diselenide ($NbSe_2$ and $ReSe_2$).

Each heterostructure is denoted as $ABSe_4$, where A and B refer to the different transition metals used. Two types of heterostructure layouts were used: 1-1 (alternating rows of $ASe_2$ and $BSe_2$) and 1-1-2-2 (one row $ASe_2$, one row $BSe_2$, two rows $ASe_2$, and two rows $BSe_2$). Thus, all lateral heterostructures were designed to keep the same chemical ratio (one-to-one for each TMD) while changing their structure. By adhering to this format, this work aims to test how increasing the in-plane symmetry breaking affects the bands. Specifically, would an increase in symmetry breaking lead to more prominent relativistic effects?

To probe such questions, Density Function Theory (DFT) is used to calculate the band structure of the 1-1 and 1-1-2-2 layouts for the $MoWSe_4$ and $NbReSe_4$ heterostructures using the Quantum Espresso software, from which energies and band structures were obtained. All scalar calculations used the PBE functional, and all relativistic calculations used the LDA functional. Each computation had an energy cutoff of 50 Ry and cold smearing of 0.005 Ry. The SCF calculations had a different k-mesh for each heterostructure: 8X8X1 for the 1-1 structure and 6X6X1 for the 1-1-2-2 structure.

Each figure has the k-path and unit cell geometry displayed to the left of the band structure. The fermi energy of the relativistic calculations was set to zero with respect to the scalar fermi energy.

## Conclusions and Future Steps:

Figure 1 details the 1-1 $MoWSe_4$ band structure. Since the fermi level is above the valence band and the band gaps of the scalar and relativistic calculations are below 2 eV (1.4697 eV and 1.3673 eV, respectively), the structure is a semiconductor.

Figure 2 describes the 1-1-2-2 $MoWSe_4$ band structure. Akin to the 1-1 structure, the fermi level is above the valence band and has scalar and relativistic band gaps below 2 eV (1.4778
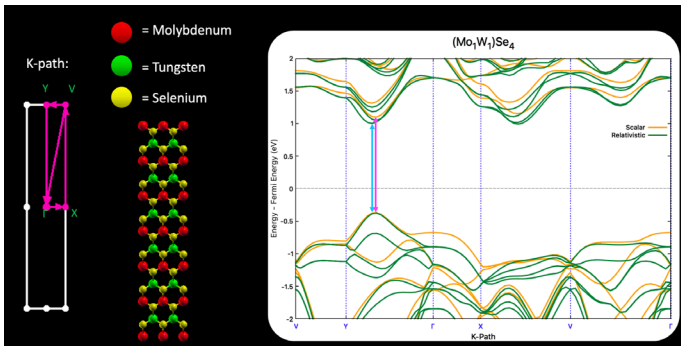
*Figure 1: Band structure of 1-1 MoWSe$_4$ with unit cell and k-path.*



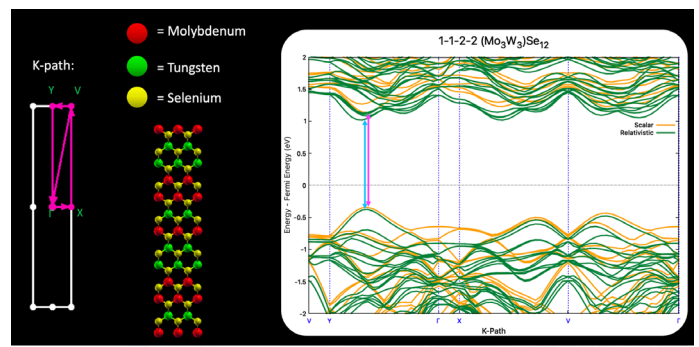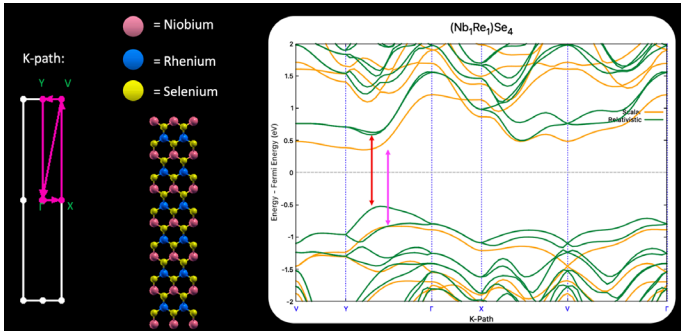*Figure 2: Band structure of 1-1-2-2 MoWSe$_4$ with unit cell and k-path.*



*Figure 3: Band structure of 1-1 NbReSe$_4$ with unit cell and k-path.*



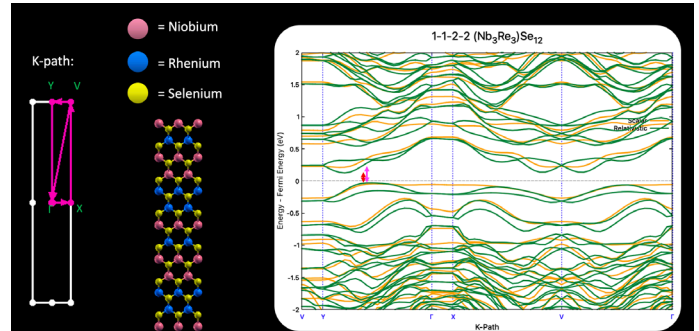*Figure 4: Band structure of 1-1-2-2 NbReSe$_4$ with unit cell and k-path.*

eV and 1.3934 eV, respectively). However, compared to the 1-1 MoWSe$_4$ structure, the band gap of 1-1-2-2 MoWSe$_4$ is slightly larger across both calculations. Additionally, the trough of the conduction band has started shifting away from the peak of the valence band, so the band structure is morphing into an indirect band gap.

Figure 3 highlights the 1-1 NbReSe$_4$ band structure. Since the fermi level is above the valence band and the band gaps are less than 2 eV (1.1869 eV and 1.093 eV for the scalar and relativistic band gaps, respectively), the system is a semiconductor.

Figure 4 shows the 1-1-2-2 NbReSe$_4$ band structure, which is quite different from the 1-1 NbReSe$_4$ structure. For instance, while the fermi level of the system is above the valence bands, the band gaps themselves are more than half their values in the 1-1 system (0.4165 eV and 0.3705 eV for the scalar and relativistic band gaps respectively). As such, this system is closer to a semimetal than a semiconductor, as the original metallic properties of the heavy core atoms are gradually enveloping the system.

Overall, an interesting trend occurs between the 1-1 and 1-1-2-2 heterostructures. Larger heterostructures have a shift in the conduction band for relativistic calculations that widens the distance between the valence band maximum and conduction band minimum in k-space, thus creating a more indirect band gap. Considering that this effect does not occur with the scalar

calculations, it seems plausible that there are increased relativistic effects in the system as heterostructure size grows.

In the future, more material compositions can be tested with varying chemical ratios to optimize for properties such as optical responsivity or electron mobility.

## References:

[1]  A. Jain, S.P. Ong, G. Hautier, W. Chen, W. Davidson Richards, S. Dacek, S. Cholia, D. Gunter, D. Skinner, G. Ceder, K.A. Persson; Commentary: The Materials Project: A materials genome approach to accelerating materials innovation. APL Mater 1 July 2013; 1 (1): 011002. https://doi.org/10.1063/1.4812323.

[2]  Ichinose, N., Maruyama, M., Hotta, H., Liu, Z., Canton-Vitoria, R., Okada, S., Zeng, F., Zhang, F., Taniguchi, T., Watanabe, K., and Kitaura, R. (2022). Two-dimensional atomic-scale ultrathin lateral heterostructures. https://arxiv.org/abs/2208.12696.

# A New Application of Metasurface Biosensors for Non-Invasive Specimens

**2023 CNF iREU Intern: Eryka Kairo**

**2023 CNF iREU Intern Affiliation: Physics, Seton Hall University**

**2023 CNF iREU Principal Investigator: Dr. Masanobu Iwanaga**

**2023 CNF iREU Mentor: Qi Hu**

**2023 CNF iREU Program Location: National Institute for Materials Science (NIMS), Tsukuba, Ibaraki, Japan**

**Contact: eryka.kairo@gmail.com, iwanaga.masanobu@nims.go.jp, qi.hu@flinders.edu.au**

## Abstract:

Recently, Dr. Iwanaga's research has focused on exploring the use of all-dielectric metasurface fluorescence (FL) biosensors, as highly effective antibody detectors, at very small concentrations. The goal of this project is to be able to detect small amounts of Immunoglobulin A (IgA) protein in a raw saliva sample, by immobilizing the protein onto a metasurface FL biosensor using the sandwich method and FL sensing. Dr. Iwanaga's lab has designed reusable metasurface FL biosensors, consisting of an all-dielectric metasurface substrate, and a microfluidic chip made of transparent polydimethylsiloxane (PDMS), which I have continued to use this summer. This project will include using a microfluidic protocol to check the sensitivity of these biosensors in salivary IgA detection and using an ELISA kit to collect data to compare the results to.

| Step | Reagent | Volume | Flow Rates | Flow Duration |
|---|---|---|---|---|
| 1 | PBS Pre-Flow | 400 µl | 600 pps | 4 minutes |
| 2 | **Cys-Streptavidin** | 100 µl | 200 pps | 5 minutes |
| 3 | PBS Rinse | 300 µl | 200 pps | 2 minutes |
| | | | 120 pps | 10 minutes |
| | | | 200 pps | 5 minutes |
| 4 | Background Measurement | | | |
| 5 | **Biotin IgA Antibody** | 100 µl | 200 pps | 5 minutes |
| 6 | PBS Rinse | 300 µl | 200 pps | 2 minutes |
| | | | 120 pps | 10 minutes |
| | | | 200 pps | 5 minutes |
| 7 | **IgA Protein** | 100 µl | 200 pps | 5 minutes |
| 8 | PBS Rinse | 300 µl | 200 pps | 2 minutes |
| | | | 120 pps | 10 minutes |
| | | | 200 pps | 5 minutes |
| 9 | **HL-555 IgA Antibody** | 100 µl | 200 pps | 5 minutes |
| 10 | PBS-T Rinse | 300 µl | 200 pps | 2 minutes |
| | | | 120 pps | 10 minutes |
| | | | 200 pps | 5 minutes |
| 11 | Yellow Fluorescent Measurement | | | |

*Figure 1: Protein times to adhere to the surface or to the protein below it.*

## Summary of Research:

The technique that we used to immobilize IgA on the metasurface long enough to image it is the Sandwich Method. The idea is to sandwich the target protein with a capture antibody, and a detector antibody that is labeled by a fluorophore. The capture antibody is a biotin-tagged IgA antibody, so that we can use Cys-Streptavidin for immobilization onto the surface. And the detector antibody is tagged with HiLyte 555 fluorescent molecules, which emit light after being excited by green incident light, signaling that IgA protein is present.

We developed a microfluidic protocol to help immobilize IgA onto the metasurface, so that we can validate that we can detect IgA using FL sensing. To control and optimize this microfluidic protocol, we used a microfluidic set-up connected to a small motor that we can control flow rates of the liquids with. The flow rates are determined based on the volume of the inlet tubes which is 150 microliters. The protocol follows the pattern of flowing the protein required and then pushing phosphate-buffered saline (PBS), giving the protein time to adhere to the surface or to the protein below it (Figure 1).

| Sample | FL Intensity |
|---|---|
| 250 ng/ml | 1204.228 |
| 50 ng/ml | 1129.112 |
| 10 ng/ml | 1065.444 |
| 2 ng/ml | 1013.250 |
| 0.4 ng/ml | 843.978 |
| 0 ng/ml | 551.116 |

*Figure 2*

To quantify and analyze fluorescent images, yellow, fluorescent images of the metasurface substrates were taken using green excitation light at intensity level 3, using a 3 second camera exposure and an electric-signal gain of 10. The FL intensities were quantified around the center of the LED illumination. We set a circular region using the image-analysis software, ImageJ, and output histograms of the FL intensities.

We took the data that we collected from the microfluidic experiment targeting a range of concentrations of IgA protein (Figure 2) and constructed a linear and semi-log graph. The linear graph had an exponential curve, and the semi-log had a linear curve, which is typical for this kind of experiment, so this experiment successfully validated that we could detect IgA at small concentrations using metasurface FL biosensors. The next step was to replace IgA with saliva in the microfluidic protocol to explore if we can target and quantify the concentration of IgA in the sample, and to perform an ELISA kit on IgA Protein to find the actual concentration of IgA in our saliva samples.

An ELISA kit is a highly accurate protein-specific quantification kit, which uses sandwich assay.

Sandwich assay is an enzyme-linked immunosorbent assay that detects and quantifies a target antigen that has been bound between two layers of antibodies, i.e., capture and detection antibodies. The technique is very similar to the Sandwich Method described earlier; the main difference is the detector antibody is linked to a color changing enzyme called HRP instead of a fluorophore. The ELISA kit helps us find the concentration of unknown samples by testing standard solutions of known concentrations of IgA so that we can create a standard curve. We tested IgA solutions of concentrations ranging from 0.78 ng/ml - 50 ng/ml and were able to form a linear curve. By using this linear curve as a guide, we can use a measured optical density and we can determine a correlated concentration. Next, we can multiply that value by our dilution factor and find the concentration of IgA in our original saliva sample.

During the next phase of experiments, we proceeded with the microfluidic protocol, and replaced IgA Protein with raw saliva, to test if we could detect IgA protein in saliva using FL sensing. For the analysis of these results, we used the exponential graph from the p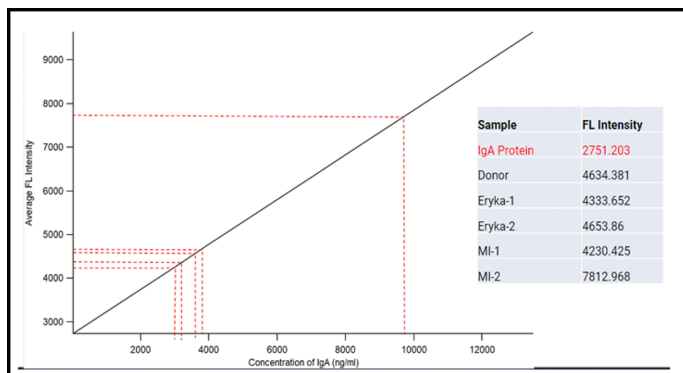revious experiment to form a standard curve using a linear curve fit function in the Igor Pro Software and created an extrapolated graph relating the concentration of IgA with the measured average FL intensity. Similarly to the ELISA kit, we can use this graph as a guide to find the concentrations of IgA in the saliva samples we tested, which you can see visually by the lines drawn on the graph (Figure 3). Mathematically we can use the linear equation of the graph to get the exact concentration measured on the metasurface substrate, and then multiply it by our dilution factor to find the concentration in the original saliva sample.

## Conclusions and Future Steps:

The final analysis step of this project is to compare the results from the microfluidic protocol targeting IgA protein in raw saliva, and the results from the ELISA protein quantification kit targeting IgA protein in raw saliva (Figure 4). The concentrations of IgA determined using the metasurface FL biosensor, was more than about 10 times higher than the concentrations determined by the ELISA kit. This inconsistency is, inferred to be due to the treatment of the saliva samples; however, this should be determined in a standard manner. Unfortunately, we are not yet sure what the issue is and moving forward we would collect more data from these experiments to draw any conclusions, and to solve the issue.

## Acknowledgements:

## References:

[1] Iwanaga M. All-Dielectric Metasurface Fluorescence Biosensors for High-Sensitivity Antibody/Antigen Detection. ACS Nano. 2020 Dec 22;14(12):17458-17467. doi: 10.1021/acsnano.0c07722. Epub 2020 Nov 24. PMID: 33231442.



*Figure 3*

| Sample | Conc. of IgA Measured in ELISA kit (µg/ml) | Conc. of IgA Measured on Metasurface (µg/ml) |
|---|---|---|
| Dr. Iwanaga | 21.713 | 293.415 |
| | | 991.930 |
| Eryka | 11.072 | 313.542 |
| | | 375.975 |
| Donor | 24.178 | 372.177 |

*Figure 4*

# Plasma-Assisted Molecular Beam Epitaxy and Electronic Transports in a SrTiO$_3$-Based Heterostructure

**2023 CNF iREU Intern: Jordana Mazer**

**2023 CNF iREU Intern Affiliation: University at Buffalo (recent graduate), University of Michigan (current student)**

## Abstract:

*In-situ* electrical measurements were performed for an oxide heterojunction unstable to the atmosphere. The molecular beam epitaxy (MBE) method was utilized and assisted with oxygen plasma to deposit barium oxide (BaO) films on an atomically smooth strontium titanate (STO) single-crystal substrates. XRD analysis confirmed the formation of epitaxial barium oxide films on the STO. After the depositions, the samples were stored in a glovebox connected to the MBE chamber and fixed in a compact microprobe system. This allowed the electrical measurements to be conducted without exposure to air, and metallic conduction was observed at the BaO/STO interface, indicating an STO-based 2-dimensional electron gas.

## Summary of Research:

**Background.** Two-Dimensional Electron Gas (2DEG) in oxide heterojunctions have been triggered by discoveries of strontium titanate (STO)-based 2DEGs. Examples of STO-based 2DEGs include lanthanum aluminate, gamma-alumina, and LSAT, all of which are formed using pulsed laser deposition (PLD) [1]. Recently, barium oxide (BaO) on STO junction was reported as a new 2DEG. One advantage of that this system has a very low lattice mismatch of -0.3%, which can be expected to make a highly crystalline interface, that can exhibit strong electrical properties [2].

Molecular beam epitaxy (MBE) is a method conducted in an ultra-high vacuum environment, keeping the samples clean and contaminant-free. MBE also enables atomic-level control in layer-by-layer growth with compositional control with better than ~ 1% accuracy. Therefore, MBE was selected for our experiments to grow BaO films.

**Goals of Project.** The main goal of this project is to observe intrinsic electron transports in the BaO/STO junctions. A challenge though is that BaO is reactive to water vapor in the atmosphere and therefore must be protected, either in a glove box or with a capping layer. The glove box allowed us to observe metallic conductive properties, while semiconducting properties were observed with a capping layer.

**Experimental Conditions.** The selected substrate used in all experiments was the STO <100> crystal with a selected growth temperature of 600°C. The oxygen partial pressure was kept at $2.5 \times 10^{-3}$ Pa and beam equivalent pressure (BEP) measurements were used to select the barium temperature of 570°C. We also did post-deposition annealing in vacuum for 1-2 hours.

Characterization methods used include X-ray diffraction (XRD), atomic force microscope (AFM), profilometry (thickness measurements), and resistivity and Hall effect measurements.

## Results and Discussion:

The first step was to treat the STO substrates so they were ready for thin-film deposition. As seen in Figure 1, AFM scans showed that as supplied, STO was a rough surface. After annealing in a furnace at 1050°C, AFM scans showed that the terracing straightened out, resulting in a much flatter surface, which is more suitable for a film to form.

Next, we deposited the barium and oxygen on the substrate, which only takes minutes, or even seconds if you want a 3 nm thin film. After deposition, the film is annealed in vacuum, without oxygen. Annealing in this environment causes an oxygen deficiency in the barium oxide layer, creating the basis for an electron transfer by the oxygen movement from the STO to the BaO, creating electrical conductivity, as seen in Figure 2. Figure 3 shows an XRD scan obtained from the BaO film on the STO substrate, where it is clearly seen that the BaO is c-axis oriented without any side products.
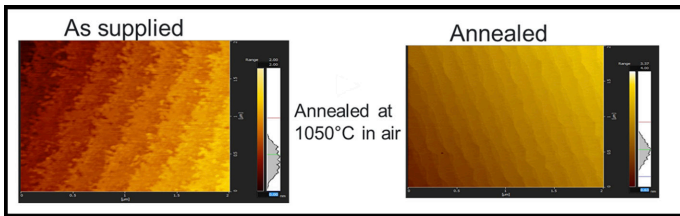
Figure 1: AFMs of the STO substrates before and after annealing in a furnace, the terracing straightened out, resulting in an atomically flat surface.
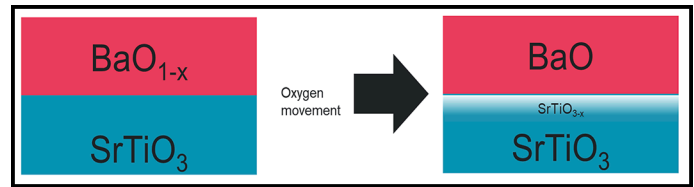


Figure 2: A schematic that shows how conductivity and electron transfer are possible.
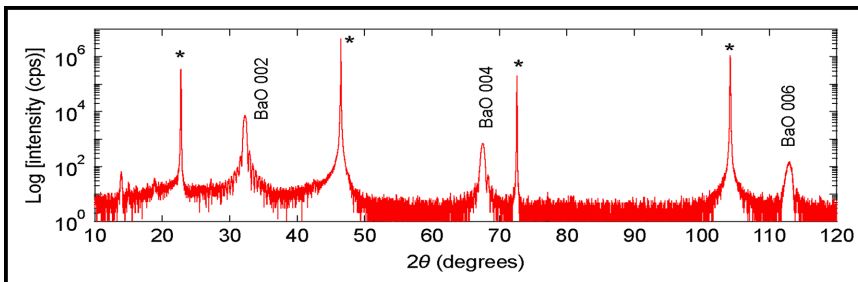


Figure 3: The XRD analysis showing the elements in STO (peaks labeled with *), and the peaks showing the formation of BaO. No side products were discovered in the film.
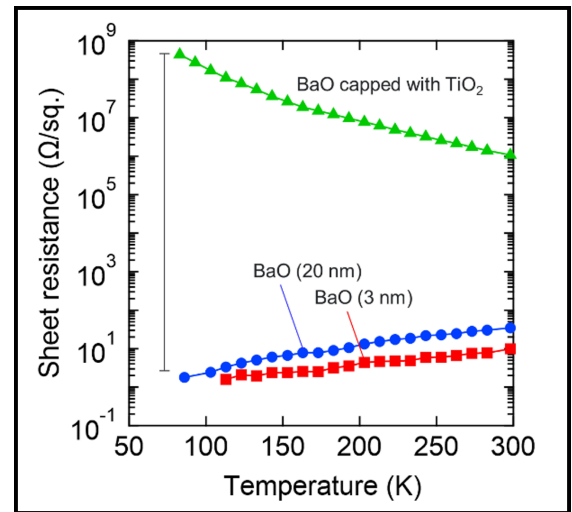


Figure 4: Resistivity measurements of the BaO/STO interface with and without a capping layer. As seen, without the capping layer, there is conductivity consistent with metallic conducting despite both STO and BaO being insulating materials on their own.

Lastly, we conducted electrical measurements. Without the capping layer, we were able to prove that conductivity exists at the interface as the resistivity pattern is consistent with metallic conductors. However, with a $TiO_2$ capping layer, the resistivity was consistent with insulating materials, as seen in Figure 4. This shows the validity of our measurement system to observe electrical properties without interference.

## Conclusions and Future Steps:

While barium oxide films were successfully deposited on atomically flat $SrTiO_3$ <100> substrates at 600°C using molecular beam epitaxy, the electrical properties observed were not constant. Resistivity displays a clear temperature-dependent pattern, but the capping layer interfered with the conducting. Future steps include improving the stability of the conductive qualities, as well as experimenting to find a capping layer that does not interfere with the electrical properties of the BaO/STO interface.

## References:

[1] Huang, Z., Ariando, Renshaw Wang, X., Rusydi, A., Chen, J., Yang, H., and Venkatesan, T. (2018). Interface engineering and emergent phenomena in oxide heterostructures. Advanced materials, 30(47), 1802439.

[2] Cao, C., Chen, S., Deng, J., Li, G., Zhang, Q., Gu, L., and Chen, X. (2022). Two-dimensional electron gas with high mobility forming at BaO/SrTiO3 interface. Chinese Physics Letters, 39(4), 047301.

# Effect of Synthesis Techniques on the Creation of Nitrogen-Vacancy Centers in Diamond

**2023 GQL IRTE Intern: Camille McDonnell**

**2023 GQL IRTE Intern Affiliation: Applied Physics, Worcester Polytechnic Institute**

**2023 GQL IRTE Principal Investigator: Dr. Tokuyuki Teraji**

**2023 GQL IRTE Mentors: Ms. Shoko Manako, Dr. Chikara Shinei, Dr. Yuta Masuyama (QST)**

**2023 GQL IRTE Program Location: National Institute for Materials Science (NIMS), Tsukuba, Ibaraki, Japan**

**Primary Sources of Research Funding: 2023 Global Quantum Leap International Research Training Experience (GQL IRTE) Program**

**Contact: cgmcdonnell8@gmail.com, teraji.tokuyuki@nims.go.jp, manako.shoko@nims.go.jp, shinei.chikara@nims.go.jp, masuyama.yuta@qst.go.jp**

**Website: https://cnf.cornell.edu/education/reu/2023**

## Abstract:

Nitrogen-vacancy (NV) centers are defects in diamond's lattice structure whose properties enable its application to quantum sensing. NV diamond quantum sensing has numerous applications including wide-field magnetic imaging, biosensing, geosensing, and quantum information systems. To make robust NV diamond sensors, they must contain a relatively high concentration of NV-centers. This project studies the effects of NV diamond synthesis and treatment techniques, specifically post annealing temperatures, on NV diamond composition with a goal of optimizing growth parameters to create better quantum sensors.

## Summary of Research:

NV centers form when a substitutional nitrogen is adjacent to a vacancy. This substitutional nitrogen (Ns) donates an electron to a neutral NV (NV0) center, creating a negative NV center (NV-) (Eq 1) [1]. A high concentration of NV-centers in diamond is necessary to make robust quantum sensors. The concentration of NV-centers and other nitrogen-related impurities can be controlled during synthesis and treatment processes. In this research, NV diamonds were synthesized using chemical vapor deposition (CVD). CVD uses hydrocarbon plasma and nitrogen gas to grow NV diamonds on a high-pressure and high-temperature NV diamond substrate [2]. CVD grown diamonds have a small concentration of NV centers compared to total nitrogen concentration; therefore, a treatment process of electron-beam (EB) irradiation and annealing is required. EB irradiation creates vacancies with a negative or neutral charge state. This concentration of vacancies is approximately equivalent to the diamond's nitrogen concentration [1]. Annealing allows for these vacancies to diffuse, causing them to be captured by Ns

$$\text{Eq 1. } N_s^0 + NV^0 \leftrightarrow N_s^+ + NV^- \quad [1].$$

to form NV centers. Previous studies have shown that vacancies begin to move at 700°C and nitrogen begin to move at 1600°C; therefore, a range of 800-1400°C is common for annealing [1]. The optimal annealing temperature is yet to be understood, which is the motivation of this research. A summary of NV diamond synthesis and treatment can be seen in Figure 1.

**Methods.** Three NV diamond samples of varying nitrogen concentration (8ppm, 4ppm, and 2ppm) were synthesized using CVD. Next, they underwent EB irradiation with an EB fluence of $5.0 \times 10^{17}$ $e/cm^2$. Finally, the samples were annealed at three different temperatures: 700°C, 1000°C, and 1400°C to determine the optimal annealing temperature. The samples were characterized after each synthesis step using optical images, photoluminescence (PL), and Fourier transform infrared (FTIR) spectroscopy. Optical images indicated external changes of the diamonds after each step, PL measured the NV-and NV0 intensity, and FTIR spectroscopy measured the Ns0 and Ns+ concentrations. After measurements, Ns0/(Ns0+Ns+) and NV-/(NV0+NV-). To confirm PL and FTIR results, a new sample with a nitrogen concentration of 8 ppm was characterized. This characterization was done using electron paramagnetic resonance (EPR) spectroscopy to measure the concentration of Ns0, negative vacancy (V-), and NV-at each synthesis step.

**Results.** The optical images of the samples indicated that the diamond became pink after 1000°C annealing (Figure 2). This likely occurred because vacancies diffused toward Ns to create NV centers. Additionally, it can be seen that the sample with higher nitrogen concentration (8ppm) was darker pink than the sample with lower nitrogen concentration (2ppm). The FTIR and PL results of the samples after each synthesis step can be seen in Figure 3. The FTIR results indicate that after EB irradiation there was a decrease in Ns0 concentration, and after annealing Ns0 concentration slightly increased. Based on Figure 1 and Eq 1, this is expected because Ns0 is used to create NV centers. Furthermore, an increase in nitrogen concentration in the sample
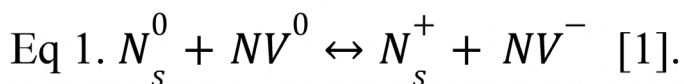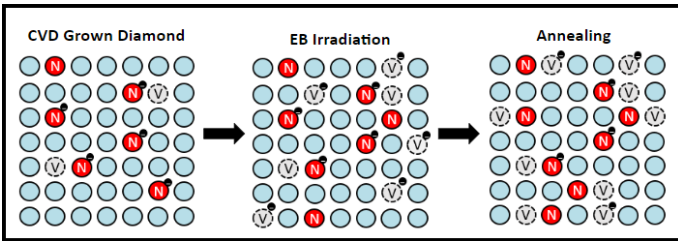
Figure 1: NV diamond synthesis and treatment procedure. Red is nitrogen and gray is a vacancy. After EB irradiation vacancies are formed, and after annealing the vacancies are diffused near Ns to create NV centers.
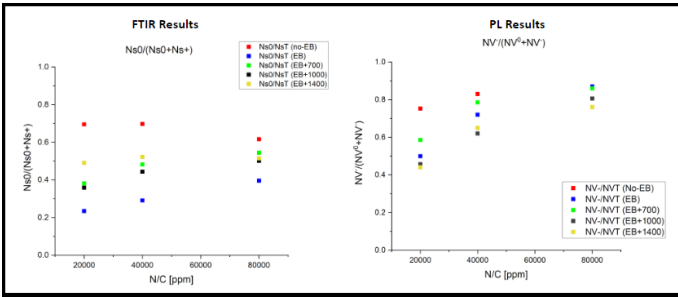


Figure 3: FTIR and PL results of each NV diamond sample after each annealing step. The unexpected data of the samples after CVD growth (No-EB) is likely due to temperature affecting measurements and a different analysis procedure used. No-EB measurements taken by Ms. Shoko Manako.

resulted in a small change of Ns0 to total Ns after each synthesis step. The PL results indicated that after each step NV0 and NV-intensity increased. To make a robust NV diamond sensor, a high concentration of NV-compared to NV0 concentration is required. Based on this requirement, the PL data concluded that an annealing temperature of 1000°C is optimal. The PL data of the No-EB sample has a very high intensity, which is unexpected. This was likely due to the data being taken prior to this project when a different analysis procedure was used. Finally, EPR data of a new 8 ppm NV diamond sample was used to confirm results of PL and FTIR (Figure 4). After EB irradiation there was a high concentration of Ns0 and V-, annealing at 800°C increased the concentration of V-compared to Ns0, and finally annealing at 1000°C resulted in a low concentration of V-and a detectable concentration of NV-. This confirmed the FTIR and PL results that 1000°C is the optimal annealing temperature.

## Conclusions and Future Work:

The results from this research determined that the optimal annealing temperature for NV diamond synthesis is 1000°C. Additionally, the FTIR and PL results show that a higher concentration of nitrogen results in a higher concentration of NV centers. Using this data, the synthesis of NV diamonds can be tailored based on their desired application, leading to the creation of better quantum sensors. To improve this research, a new set of samples grown at the same concentration should be studied to confirm these results. Furthermore, studying a new set of samples will help confirm the unexpected PL data that was
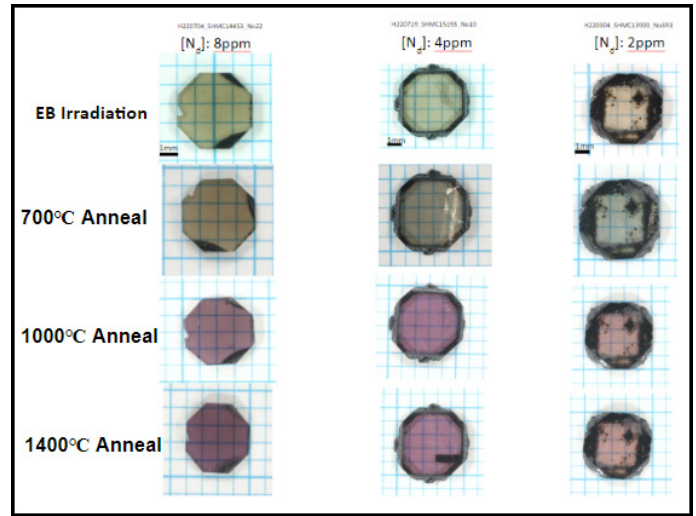


Figure 2: Optical images of NV diamond samples at each synthesis step. After annealing at 1000°C, the samples change from a yellow/brown color to pink.
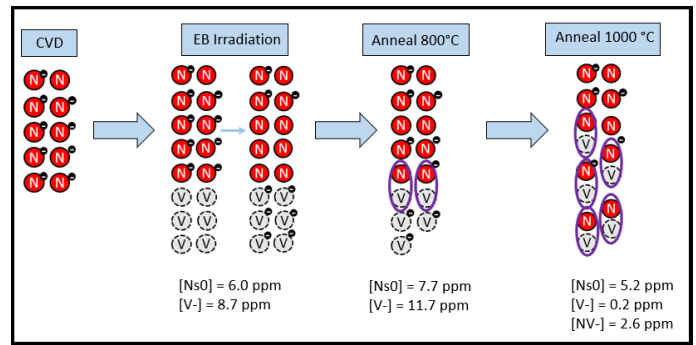


Figure 4: EPR results of an 8ppm diamond sample confirmed that the optimal annealing temperature is 1000°C. Red is nitrogen, gray is a vacancy, and purple is an NV center. Measurements taken by Dr. Chikara Shinei.

measured after CVD growth. Finally, to better understand the properties of the samples and how they can be used as optimal quantum sensors, their coherence properties should be measured using optically detected magnetic resonance.

## References:

[1] Shinei, C., et al. (2021). Equilibrium charge state of NV centers in diamond. Applied Physics Letters, 119(25), 254001. https://doi.org/10.1063/5.0079687.

[2] Barry, J., et al. (2020). Sensitivity optimization for NV-diamond magnetometry. Reviews of Modern Physics, 92(1), 015004. https://doi.org/10.1103/RevModPhys.92.015004.

# Ball-Milling Synthesis Investigation of a-MgAgSb to Enhance Thermoelectric Properties and Reproducibility

**2023 CNF iREU Intern: Steph Meikle**

**2023 CNF iREU Intern Affiliation: Materials Science and Engineering, University of Florida**

**2023 CNF iREU Principal Investigator: Dr. Takao Mori**

**2023 CNF iREU Mentor: Dr. Song-Yi Back**

**2023 CNF iREU Program Location: National Institute for Materials Science (NIMS), Tsukuba, Ibaraki, Japan**

**Primary Sources of Research Funding: 2023 Cornell NanoScale Facility International Research Experiences for Undergraduates (CNF iREU) Program via the National Science Foundation Grant No. NNCI-2025233**

**Contact: steven.meikle@ufl.edu, mori.takao@nims.go.jp, back.songyi@nims.go.jp**

**Website: https://cnf.cornell.edu/education/reu/2023**

## Abstract:

Unideal multi-step synthesis and challenges regarding the reproducibility of high-performing $\alpha$-MgAgSb has set precedent for modifying high energy ball-milling synthesis procedures to improve its thermoelectric properties. Refining efforts to regulate the presence of impurity phases (e.g., $Ag_3Sb$, AgMg, Sb, and $Mg_{54}Ag_{17}$) by time-effective phase content control has been reported in literature, but synthesis optimization remains relatively unexamined. In this work, we demonstrate that a high ZT of 1.21 at 423 K for $MgAg_{0.97}Sb_{0.99}$ can be obtained by high energy ball-milling of Mg and Ag for ten hours and by later incorporating Sb for five hours, proceeded with six hours of annealing at 573 K. Ongoing investigation of this study revealed a potential maximum ZT of 1.36 at 473 K. The $\alpha$-MgAgSb:Sb ratio exhibited was 98.52:1.48% with no other impurity phases present. Fine tuning Sb particle size may affect precursor mixing homogeneity, evidenced by gradual thermoelectric property improvement in this study. Achieving this ratio of $\alpha$-MgAgSb and secondary-phase Sb with this simpler synthesis process makes way for employing MgAgSb as thermoelectric materials.

## Introduction and Background:

High performing thermoelectric (TE) materials for power generation at low temperatures remain of interest for mitigating usable heat loss in a wide variety of energy systems. The dimensionless figure of merit, $ZT = S^2\sigma T\kappa^{-1}$, where S is the Seebeck coefficient, $\sigma$ is the electrical conductivity, T is the absolute temperature, and $\kappa$ is the total thermal conductivity, characterizes the thermoelectric performance of a material or device. According to Zhihang et al., $\alpha$-MgAgSb ($I\bar{4}2c$) can exhibit a high ZT ranging from 1.2 to 1.4, though at 550 K [1]. A trade-off between the temperature-dependent S, $\sigma$, and $\kappa$ exists to achieve high performance, prompting multifaceted investigation of the effects of synthesis modification on TE properties. For instance, enhancing S2$\sigma$, otherwise known as the power factor (PF), while suppressing lattice thermal conductivity $\kappa_L$ is imperative for maintaining a high ZT.

In this study, we investigate the effects of ball-milling time steps on MgAgSb phase ratios and S, PF, ZT, $\kappa_L$, electrical resistivity ($\rho$), total thermal conductivity ($\kappa$), and weighted mobility ($\mu_W$). The MgAgSb alloys were prepared by one-step and two-step high energy ball-milling. Mg and Ag milled first for the two-step process, later introduced with Sb particles on the second step. Spark plasma sintering (SPS) and thermal annealing proceeded, to induce phase transitions at a maximum temperature of 300K. Results provided insight on how phase composition can be tuned through honing the order or duration of ball-milling time steps. Shorter and less involuted ball-milling time steps without the need for defect or band structure engineering can provide a simpler route to synthesizing high-ZT $\alpha$-MgAgSb.

## Results and Summary:

Figure 1 contains XRD patterns of samples A-H, revealing the effects of high energy ball-milling step changes on MgAgSb phase content. The following sample names correspond with the following ball-milling time steps and Sb sizes: i) A = 5 hours, ii) B = 5 hours and 5 hours, iii) C = 10 hours, iv) D = 10 hours and 5 hours, v) E = 5 hour and 5 hours, with crushed Sb, vi) F = 10 hours and 5 hours, with crushed Sb, vii) G = replicate of F, and viii) H = 10 hours, with crushed Sb. Sample F had the highest relative peak intensity with minimal broadening at 23.8° 2Θ, whereas samples A, B, C, and H exhibited slight peak broadening. The impurity phase AgMg was identifiable in all samples, except E and F, with $Mg_{54}Ag_{17}$ being present in only A, B, and H. Peaks attributed to impurity phases were more prominent in samples subjected to the one-step for five hours, two-steps for five hours, and one-step for ten hours procedures, indicating a lack of AgMg precursor phase to $\alpha$-MgAgSb transitions. Depending on
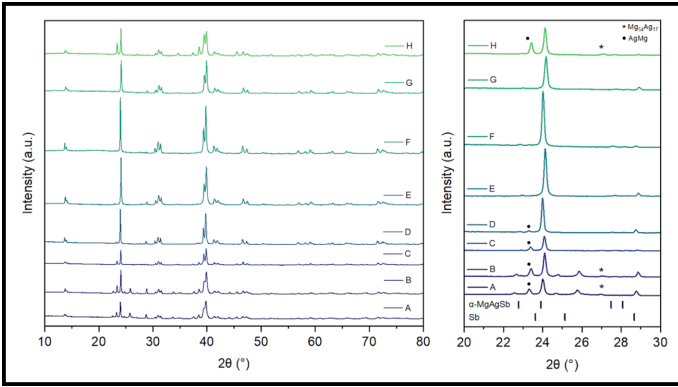
*Figure 1: (Left) XRD patterns and (Right) 20°-30° 2Θ range of MgAg$_{0.97}$Sb$_{0.99}$ samples A-H. Relevant Bragg positions for α-MgAgSb and Sb are shown at the bottom for reference (Right).*
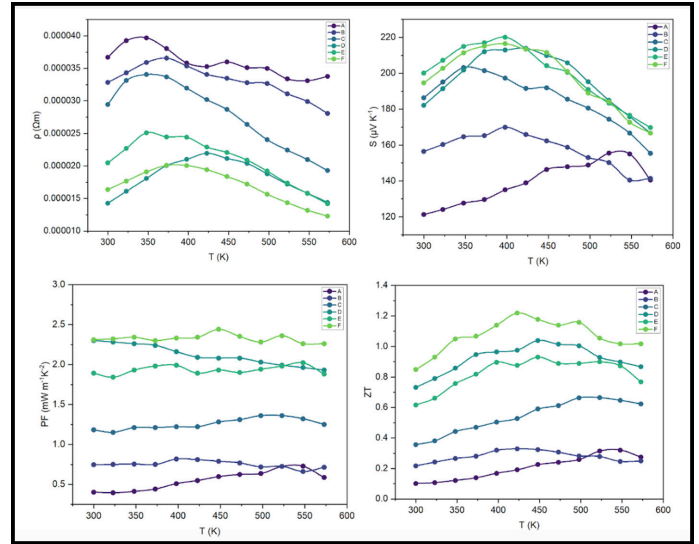


*Figure 2: Electrical resistivity (ρ), Seebeck coefficient (μVK$^{-1}$), power factor (mW m$^{-1}$K$^{-2}$), and ZT vs. temperature.*

the initial phases formed during the first milling step and the duration of the second milling step, desirable phases whereby $\kappa_L$ is minimized and ZT is maximized may form, as evidenced by the XRD patterns and TE properties for samples E and F.

Figure 2 provides insight on the thermoelectric properties against temperature, with samples A-F being investigated. The ρ vs. T plot revealed that sample F exhibited the lowest electrical resistivity, with only a peak resistivity of 2.007E-5 Ωm at 373K. Sample F's peak high Seebeck coefficient of 216.35 μV K$^{-1}$ at 398K and power factor of 2.44 mW m$^{-1}$K$^{-2}$ at 448 K gives rise to sample F's high ZT value. Electrical resistivity can simply be represented as ρ = σ$^{-1}$, in accordance with the Drude-Sommerfeld free electron model.

Therefore, it is possible that sample F exhibited comparably larger σs enabling for the minimization of ρ, thus improving the power factor given that PF = S$^2$σ. Sample F's comparably high Seebeck coefficient also contributed to a high PF, though the magnitude of each S and σ contribution is dependent on temperature. Sample F was able to achieve a ZT of 1.04 at 348K, with a peak ZT of 1.22 at 423K. Though an ongoing investigation, replicate sample

G demonstrated a maximum ZT of 1.36 at 473K, thus indicating reproducibility of thermoelectric properties despite slight phase impurity ratio changes. In conclusion, ZT values were successfully increased by controlling BM procedures. Compared to other complex and time-consuming procedures, this synthesis is quite simple and effective to obtain high ZT samples.

## Acknowledgements:

## References:

[1] Liu, Zihang, et al., "High Thermoelectric Performance of α-Mgagsb for Power Generation." Energy and Environmental Science, The Royal Society of Chemistry, 18 Oct. 2017.

# Cytotoxic Effect of Epidermal Growth Factor-Gold Nanoparticle Conjugates

**2023 CNF iREU Intern: Ryan Barcelona Talusan**

**2023 CNF iREU Intern Affiliation: Bioengineering, University of Illinois at Urbana-Champaign**

**2023 CNF iREU Principal Investigator: Professor Jun Nakanishi**

**2023 CNF iREU Mentor: Dr. Shota Yamamoto**

**2023 CNF iREU Program Location: National Institute for Materials Science (NIMS), Tsukuba, Ibaraki, Japan**

**Primary Sources of Research Funding: 2023 Cornell NanoScale Facility International Research Experiences for Undergraduates (CNF iREU) Program via the National Science Foundation Grant No. NNCI-2025233**

**Contact: rtalus2@illinois.edu, nakanishi.jun@nims.go.jp, yamamoto.shota@nims.go.jp**

**Websites: https://cnf.cornell.edu/education/reu/2023, https://www.nims.go.jp/group/mechanobiology/**

## Abstract:

Cancer cells stemming from an overexpression of the epidermal growth factor receptor (EGFR) surface protein expression often develop resistance to conventional EGFR inhibitors. Epidermal Growth Factor-Gold Nanoparticle (EGF-GNP) conjugates offer a potential alternative, demonstrating significant cytotoxicity against drug-resistant cells at different diameters (60 nm, 80 nm, and 200 nm) when compared to media. While the exact mechanism remains unclear, optimizing the nanoparticle's effectiveness could provide patients with a valuable additional cancer-fighting option.

## Summary of Research:

**Background and Motivation.** Epidermal growth factor receptor (EGFR) is a vital cell surface protein involved in signaling pathways within human cells, impacting functions like cell proliferation, inflammation, and extracellular matrix regulation [1]. Dysregulation of EGFR signaling contributes to excessive cell growth, cancer progression through processes like angiogenesis and metastasis, and resistance



*Figure 1: A graphic highlighting the advantages of EGF-GNP.*

to apoptosis [2]. EGFR inhibitors are developed to block its activation and hinder tumor cell proliferation, but they come with notable side effects, including folliculitis, xerosis, pruritus, and alopecia [3]. Resistance often develops, especially after epithelial-mesenchymal transition or EGFR mutations occur, posing challenges in treating EGFR-driven cancers. To address this, researchers have explored conjugating Epidermal Growth Factor (EGF) to gold nanoparticles (GNP) to reduce cancer cell viability, with previous studies showing cytotoxicity at 15 and 50 nm [5,6]. This study aims to investigate how the size of Epidermal Growth Factor-Gold Nanoparticle (EGF-GNP) conjugates affects their cytotoxicity against cancer cells.
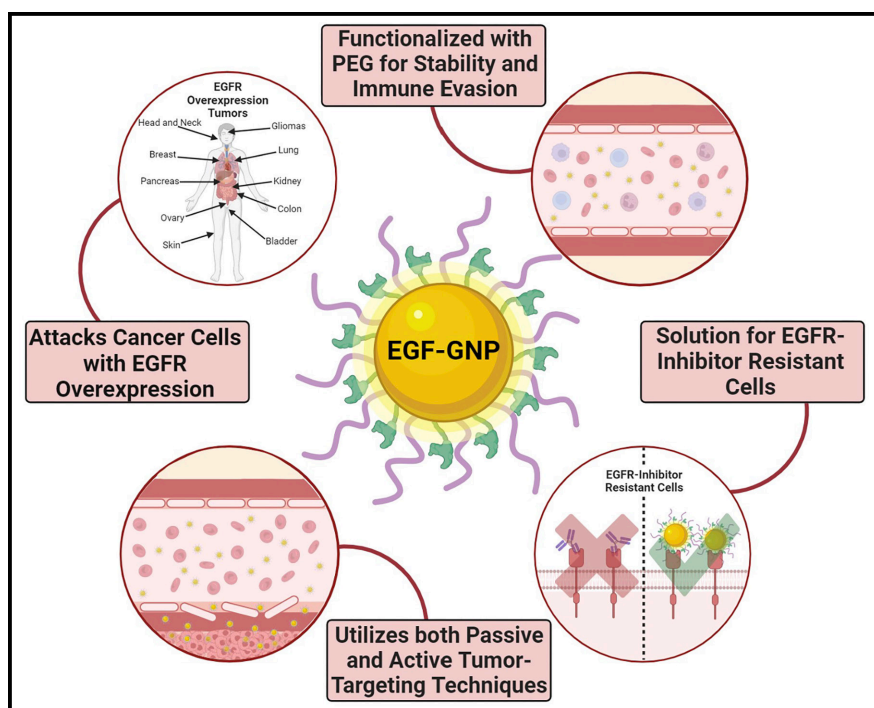
**Materials and Methods.** Epidermal growth factor-nanoparticle conjugates were prepared as per established methods [7]. Growth analysis between functionalization was done to confirm successful conjugation. Initially, GNPs were functionalized with PEG-DSU and HS-PEG-COOH, introducing PEG for stability and immune evasion, thereby forming PEG-GNP, as shown in Figure 2 [8]. Subsequently, EDC/NHS was used to activate HS-PEG-COOH's carboxyl group, enabling EGF binding and creating EGF-GNP, as shown in Figure 2. DLS measurements at each functionalization step showed a significant size increase, validating successful conjugation of EGF. Following functionalization, both EGF-GNP and PEG-GNP of various hydrodynamic diameters
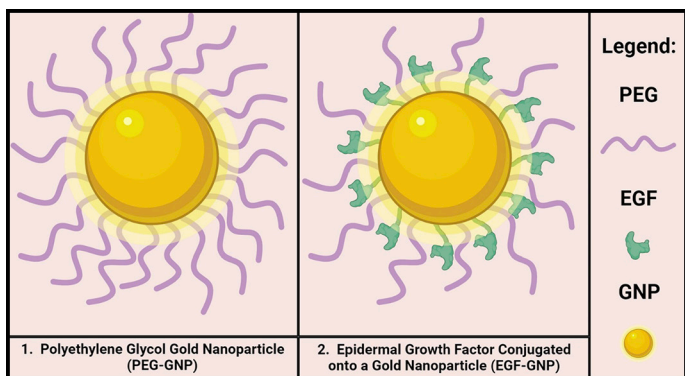
Figure 2: A graphic showcasing the functionalization of PEG and conjugation of EGF onto the GNP.
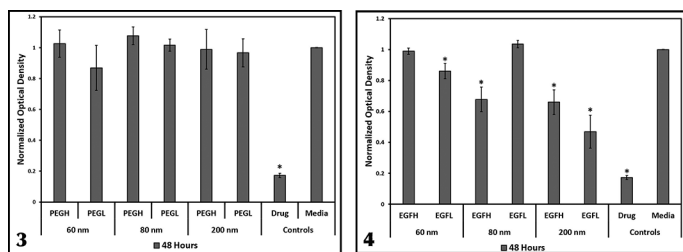


Figure 3, left: Normalized optical density of all PEG-GNP samples after 48 hours. The asterisk above drug represents a significant difference against the media. Figure 4, right: Normalized optical density of all EGF-GNP samples after 48 hours. The asterisk above certain conditions represents significant difference against the media.

(60 nm, 80 nm, and 200 nm) were introduced to cancer cell cultures at high and low concentrations, with the former having ten times the GNPs. After 48 hours of incubation, Cell Counting Kit-8 was used to quantify live cancer cells, and a microplate reader measured optical density differences for each condition. Due to the GNP's ability to absorb and scatter light efficiently, controls were set in place to subtract the effect of the GNP on the optical density.

**Results and Discussion.** To explore the cytotoxicity related to EGF-GNPs' size, we compared them to PEG-GNPs of the same diameter and media. The optical density in each sample was normalized against the media to emphasize the impact of each condition. Figure 3 indicates that none of the listed conditions significantly differed from the media, which aligns with expectations since PEG's presence shouldn't induce cytotoxicity. However, some EGF-GNP conditions exhibited statistically significant decreases in cell viability, as shown in Figure 4. Incubation with 60-EGFL, 80-EGFH, 200-EGFH, and 200-EGFL resulted in notable reductions in optical density and, consequently, cell viability. Even though 80-EGFL's optical density appears similar to the media, it's likely that this is an outlier and replicating this experiment would reveal a reduction in measured optical density.

These findings align with current research regarding the impact of EGF on cell viability and support the claim that EGF is solely responsible for the cytotoxic effects.

## Conclusions and Future Steps:

The novelty of this project arises from the significant enhancement in cytotoxic efficiency while increasing GNP diameter. Although the exact cytotoxic mechanism remains unknown, it is believed that the increase in surface area from GNPs with larger diameters allows for greater PEG and EGF functionalization, increasing the potential for EGF-GNP binding to EGFR and subsequent cytotoxic effects. Future research can focus on enhancing EGF-GNP by modifying PEG molecular weight,

adjusting EGF or PEG surface densities, exploring more diameters, or varying incubation times. Ultimately, gaining insights into the underlying cytotoxic mechanisms and using this knowledge to optimize this technology would offer a safer alternative for treating cancers driven by EGFR overexpression, benefiting patients.

## References:

[1] Rayego-Mateos, S., et al. Role of Epidermal Growth Factor Receptor (EGFR) and Its Ligands in Kidney Inflammation and Damage. Mediators Inflamm 2018, 8739473 (2018).

[2] Sasaki, T., et al. The Role of Epidermal Growth Factor Receptor in Cancer Metastasis and Microenvironment. BioMed Research International 2013, e546318 (2013).

[3] Hirsh, V. Managing treatment-related adverse events associated with EGFR tyrosine kinase inhibitors in advanced non-small-cell lung cancer. Curr Oncol 18, 126-138 (2011).

[4] Weng, C.-H. et al. Epithelial-mesenchymal transition (EMT) beyond EGFR mutations per se is a common mechanism for acquired resistance to EGFR TKI. Oncogene 38, 455-468 (2019).

[5] Zhang A, Nakanishi J. Improved anti-cancer effect of epidermal growth factor-gold nanoparticle conjugates by protein orientation through site-specific mutagenesis. Sci Technol Adv Mater. 2021 Sep 6;22(1):616-626. doi: 10.1080/14686996.2021.1944783. PMID: 34512175; PMCID: PMC8425683.

[6] Yamamoto S, Nakanishi J. Epidermal Growth Factor-gold Nanoparticle Conjugates-induced Cellular Responses: Effect of Interfacial Parameters between Cell and Nanoparticle. Anal Sci. 2021 May 10;37(5):741-745. doi: 10.2116/analsci.20SCP16. Epub 2020 Dec 25. PMID: 33390415.

[7] Wu L, Xu F, Reinhard BM. Nanoconjugation prolongs endosomal signaling of the epidermal growth factor receptor and enhances apoptosis. Nanoscale. 2016 Jul 14;8(28):13755-68. doi: 10.1039/c6nr02974d. PMID: 27378391; PMCID: PMC5081566.

[8] Li, M., et al. Brush Conformation of Polyethylene Glycol Determines the Stealth Effect of Nanocarriers in the Low Protein Adsorption Regime. Nano Lett. 2021 Feb 24;21(4):1591-1598. doi: 10.1021/acs.nanolett.0c03756. Epub 2021 Feb 9. PMID: 33560851; PMCID: PMC8023711.

# Nanomechanical Membrane-Type Surface Stress Sensor: A Case Study on Device Optimization and Food Samples

**2023 CNF iREU Intern: Stephanie Wang**

**2023 CNF iREU Intern Affiliation: Case Western Reserve University**

## Abstract:

One approach of artificial olfaction looks at the unique combination of vapor molecules that constitute an odor to smell receptors in animals. Nanomechanical sensors, especially those that functionalize microcantilevers, are highly effective in identifying and quantifying these gaseous releases. One of the optimized nanomechanical sensors, the nanomechanical Membrane-Type Surface stress Sensor (MSS) shows promising results. The MSS module was studied to determine optimal measuring parameters due to its highly sensitive nature. The module is affected by environmental factors such as temperature and humidity, so these were monitored and minimized. Signal data from the MSS on various food samples were gathered for comparison as well as future reference.

## Summary of Research:

**Sensing Technology.** The sensing platform on the MSS module comprises of silicon microfabricated sensors. At the edge of the sensors are embedded piezoresistors. As gas molecules flow through the system, they adsorb onto the sensors, causing mechanical deflection. This induces stress on the piezoresistors and changes their electrical resistance. The voltage across this resistance is the output signal, unique to the sample being measured. In this study, eight different receptor layers were used, resulting in eight different output signals from each channel. The module also has humidity and temperature channels.



Figure 1: Measurement system depicting connections and airflow.

**Measurement System.** First, a new measurement system had to be built as shown in the schematic of Figure 1. A line of nitrogen was connected to the system due to its inert nature. It will not react with samples, altering the gaseous composition and skewing data. The flow of nitrogen from a gas tank is set by a mass flow controller (MFC). The sample is connected to the sampling side of the module. Nitrogen is also connected to the purging side of the module. This ensures that molecules adsorbed to the sensors from the previous run can be removed before sampling again. One line is left open from the nitrogen. This ensures that the gas flow from the tank and the settings on the module match up. It also decreases humidity within the system since the MFC is purposely set at a higher flow rate compared to the module. To control temperature, the module is placed in an incubator set at 25°C. All connections were tight and checked often to prevent any air leakages.

**Samples.** The tested substances were all consumable and ranged from solids to liquids. Water was first tested for practice, ensuring consistent and replicable results. Other liquids included tea, coffee, milk, juice, and soda. Solids tested were matcha powder, coffee grounds, and chocolate.

**Measurement Technique.** Each substance tested was sampled for one minute. Purging lasted four minutes to ensure that there were no remaining residues from the previous sample. Sampling was repeated four times for each substance. The total testing time per sample was 20 minutes. Multiple trials of the same sample were performed as well. Data was analyzed and graphed using software coded specifically for the MSS module.

**Results.** Initial tests were run with water in the sampling vial. The goal was to achieve reproducibility by generating the almost equivalent signals across different trials of DI $H_2O$. Identical signals, however, are difficult to output due to sensors' high sensitivity. One major environmental factor is humidity. In Figure 3, the humidity channel shows a significant difference between two trials of chocolate. Temperature, on the other hand, is quite stable across the two trials, ranging from 30.6-30.7°C. The output signal of channel 3 shows that higher humidity increases
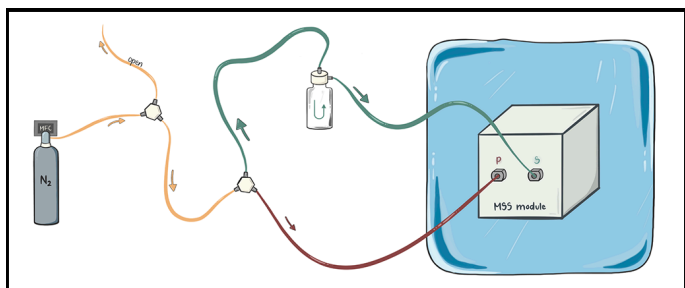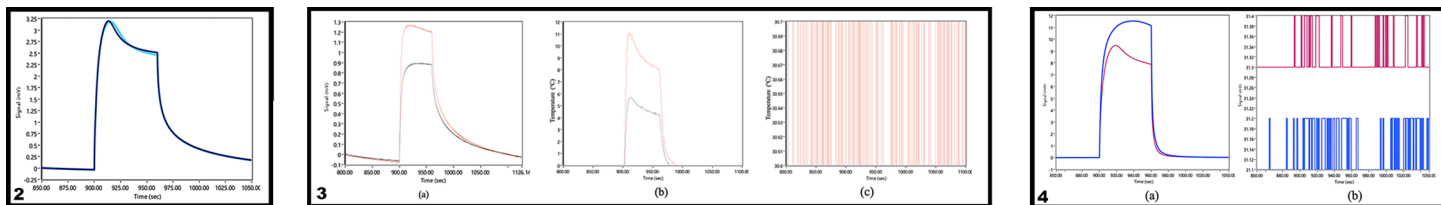
Figure 2: Channel 2 signal of two separate water samples. Figure 3: (a) Channel 3 signal of two different trials testing dark chocolate. (b) Humidity signal corresponding to dark chocolate samples in 4a. (c) Steady temperature signal of above samples. Figure 4: When humidity is stable, but temperature varies, the shape of the voltage signal will vary as shown in Figure 4a.

the voltage magnitude across the resistors due to increased resistance from mechanical deformation. Temperatures are variable and greater than the incubator's set temperature at 25°C. This is due to the pump within the module that generates heat, and it removes contaminated air and location of the sample vials outside the incubator. Samples must be changed out manually, so they cannot be placed inside or else the incubator will have to be opened, defeating its purpose.

The second major factor of concern is temperature. When humidity is stable, but temperature varies, the shape of the voltage signal will vary as shown in Figure 4a. Even a change of 0.3°C can result in a significant change in the output. This is due to samples with different conditions and sensing conditions.

Once more precise signals were achieved, different samples were compared to one another. Principal component analysis (PCA) was performed by placing a cursor on the compilation of signals on the left of Figure 5. Data from every channel for each signal was extracted at the cursor. This data was analyzed using MSS-specific software to generate the principal component graph below. Principal component 1 (PC1) is on the x-axis and PC2 is shown on the y-axis. Here we can distinguish between the different samples tested, which the PCA graph being more readable compared to the output signal information.

## Conclusions and Future Work:

We were able to develop a method of extracting data that are reproducible and beneficial in various industrial applications. Using the MSS module, however, still requires a high attention to detail. Regular check-ups on connections within the system are imperative to preventing leaks. Additionally ensuring constant humidity and temperature is crucial for reliable results.

The ability of MSS to test everyday consumables in the form of both liquids and solids is useful in the food

industry. Ripeness of produce can be differentiated by the "smell" or hormones released. There are so many applications aside from food, such as testing expiration of make-up products in the beauty industry and testing breath of patients for illness detection in health settings.
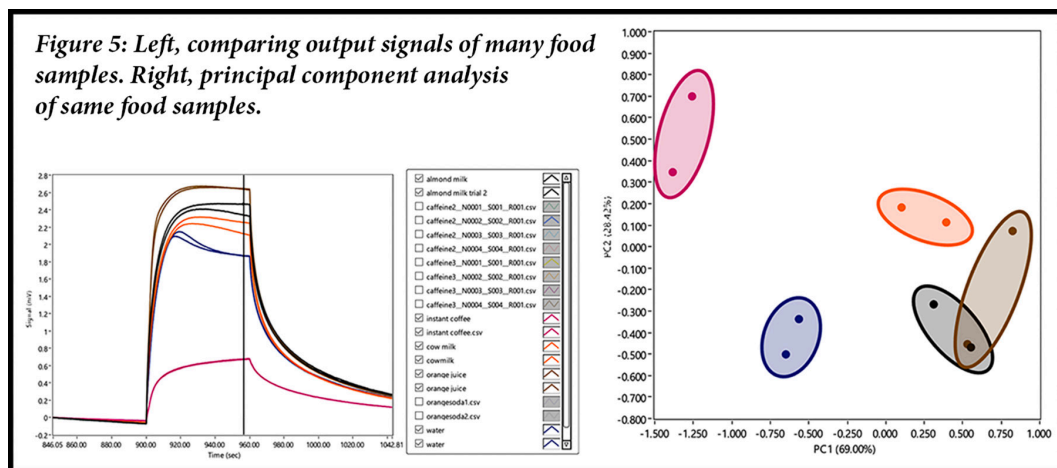
Future work can also be done to improve the capability and reliability of the MSS. For example, adding another MSS and having two lines of nitrogen flowing from the source will make sure there is no backflow of air during purging and decreased the humidity. In the current system, samples are not incubated, which caused some temperature fluctuations. Otherwise, the incubator would have to be opened during sample changing. Placing the entire in an incubated glove box could be a solution to this problem.

## Acknowledgements:

## References:

[1] Minami, Kosuke, et al. Biosensors vol. 12,9 762. 16 Sep. 2022, doi:10.3390/bios12090762.

[2] G. Imamura, K. Shiba, and G. Yoshikawa, Japanese Journal of Applied Physics 55, 1102B1103 (2016).

Figure 5: Left, comparing output signals of many food samples. Right, principal component analysis of same food samples.

# 2023 CNF Japan Programs Final Reports

# INDEX

## 2023 Japan Programs

**These reports are online at https://www.cnf.cornell.edu/ education/international**